

# Evaluation of particle motions in stabilized specimens of transparent sand using deep learning segmentation

David Marx<sup>1\*</sup>, Krishna Kumar<sup>1</sup> and Jorge Zornberg<sup>1</sup>

<sup>1</sup> Department of Civil Architectural and Environmental Engineering, The University of Texas at Austin, United States of America.

\*Corresponding author: dawie.marx@utexas.edu

## Abstract

Individual particle rotation and displacement were measured in triaxial tests on transparent sand stabilized with geogrid simulants. The Cellpose U-Net model, originally developed to segment biological cells, was trained to segment images of fused quartz particles. The Score-CAM metric from the field of Explainable AI was used to validate the application of Cellpose to segment particles of fused quartz. These segmented particles were characterized in terms of Fourier shape descriptors and tracked across images. The measured particle displacements in the monotonic triaxial tests correlated with displacement fields from Digital Image Correlation (DIC). In contrast to DIC, the new technique also allows for the measurement of individual particle rotation. The particle rotation measurements were found to be repeatable across different specimens. A state boundary line between probable and improbable particle motions could be identified for a given test based on the measured particle displacements and rotations. The size of the zone of probable motions was used to quantify the effectiveness of the stabilizing inclusions. The results of repeated load tests revealed that the honeycomb inclusions used stabilized the specimens by reducing both particle displacements and rotations.

**Keywords:** transparent sand, stabilization, deep learning, segmentation, triaxial testing

## 1. Introduction

An understanding of soil-geogrid interaction is critical for evaluating the performance of a geogrid in engineering applications. Measurement of soil-geogrid interaction in literature spans from the macro-scale to the meso-scale to the micro-scale. Macro-scale measurements of the ultimate strength of reinforced specimens or the accumulated permanent strain of stabilized specimens are routinely taken in triaxial tests. At the meso-scale, the local stiffness of stabilized triaxial specimens has been successfully measured with bender elements (Byun and Tutumluer, 2017; Kang et al. 2020). Kharchafi and Dysli (1993) and Alagiyawanna et al. (2001) investigated soil-geosynthetic interaction by measuring the displacement of a discrete grid of lead short markers embedded in the soil with X-ray radiography. At the microscale, Zhou et al. (2012) and Abdi and Mirzaeifar (2017) made particle level measurements of displacement using digital image correlation. In addition, particle level studies can be done using either Discrete Element Modelling (DEM) with geosynthetic inclusions (e.g. McDowell et al., 2006; Ngo et al., 2014) or microtomography of unreinforced specimens (e.g. Hall et al., 2010). However, DEM limited by the quality of the calibration (Coetzee, 2017), while microtomography is restricted to discrete measurements on miniature specimens.

This paper discusses a technique to take high frequency measurements of particle-level motions in 50 mm stabilized triaxial specimens of transparent sand. A deep neural network was used to segment images of the triaxial specimens into individual particles. These particles were subsequently tracked throughout the testing by matching their Fourier descriptors. This facilitates measurement of individual particle displacement and rotation in the presence of stabilizing inclusions.

## 2. Experimental program

### 2.1. Experimental setup

A conventional triaxial cell and load frame were placed inside a custom imaging frame. Key elements of the imaging frame such as the alignment markers, cameras, and lasers are indicated in **Figure 1** (the load frame, oil-water interfaces, and volume pumps are not shown).

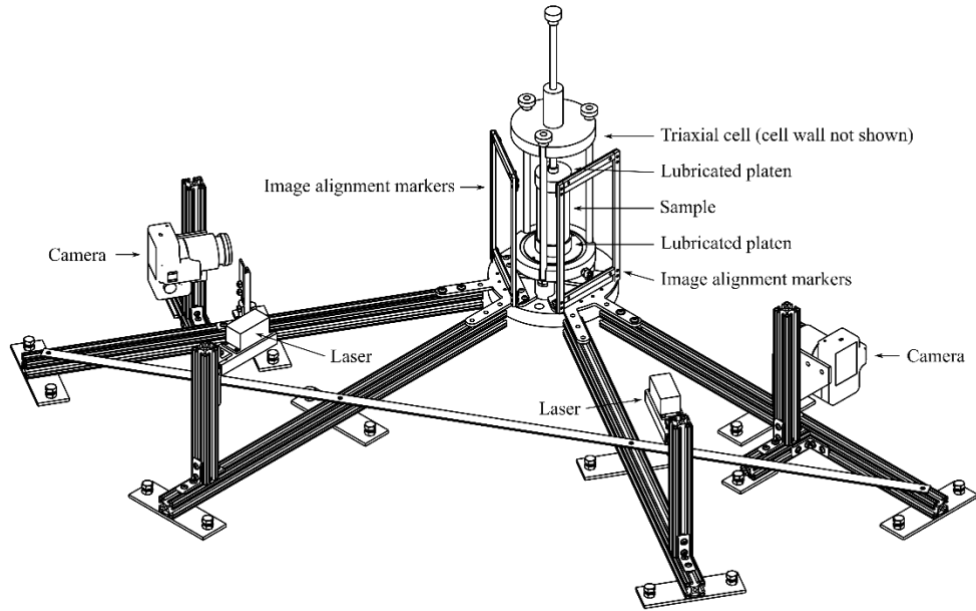


**Figure 1.** Experimental setup

Two lasers, a 350 mW and a 450 mW laser, both with a wavelength of 638 nm, were placed at  $60^\circ$  relative to each other. At  $90^\circ$  relative to each of the lasers, a Canon EOS 5DS R camera fitted with a Sigma 50 mm f/1.4 lens was positioned to track particle motion across two intersecting planes inside the specimen. Red LEDs were used following Stanier (2012) to align the images in the event of slight camera motion during the testing. The details of this experimental setup are not the focus of this paper, and additional information will be available in separate publication.

### 2.2. Transparent sand

Transparent sand is manufactured by index matching fused quartz with mineral oil (Ezzein and Bathurst, 2011). Due to the matching refractive indices, light transmits through the specimen, rather than reflecting at the particle surfaces. Thus, the specimen is transparent.

A perfect match in refractive indices is rare. The inevitable minor mismatch can be exploited by illuminating a section through the sample using a sheet laser. The laser refracts at the particle edges, brightening them and allows for individual particles to be tracked (Sadek et al., 2003; Peng and Zornberg, 2019; Derksen et al., 2022). This technique is limited by the depth of visibility, which is influenced by the presence of air bubbles and contaminants, the quality of the refractive index match, and the number of particle surfaces between the observer and the section of interest (Black and Take, 2015).

In this study, a uniformly graded fused quartz was used in this study to improve the clarity of the particle outlines. The sand had a  $D_{50}$  of 2.9 mm and a minimum and maximum void ratio of 0.72 and 0.85, respectively (ASTM D4253-16, ASTM D4254-16). The particles are highly angular and flakier than spherical. Therefore, while the smallest particle dimension is 2.9 mm, the largest can measure up to 5 mm in diameter. The fused quartz was saturated with a mixture of two oils: 52% Puretol 7 Special and 48% Paraflex HT4, both manufactured by Petro-Canada (Peng and Zornberg, 2019).

### 2.3. Inclusions

When a geogrid is placed in a ballast layer or a road subbase, the function is typically to stiffen the unbound aggregate layer, reducing rutting or settlement, rather than preventing ultimate collapse. In this study, the performance of the geogrid simulants (inclusions) was evaluated in terms of the permanent strain that accumulated in the specimens, rather than the ultimate strength achieved. Consequently, the specimens are considered stabilized, rather than reinforced.

A stabilized triaxial specimen cannot be considered a true unit cell, as the stress state across the inclusion is discontinuous. However, a triaxial test does allow for soil-geogrid interaction to be studied under consistent boundary conditions. As the stress state in a triaxial specimen is axisymmetric, an inclusion should provide axisymmetric stabilization for compatibility.

An annular inclusion is the simplest geometry that provides axisymmetric stabilization. However, if a thin ring is used for stabilization, only a limited volume of soil will interact with the geogrid. Two concentric rings can be used to increase the confinement; however this leads to greater confinement in the radial direction than the circumferential direction. The simplest geometric pattern, other than a ring, that provides equivalent confinement in both the radial and the circumferential directions is a honeycomb pattern.

The two types of honeycomb inclusions shown in **Figure 2** were used for stabilization in this study. These inclusions were cut from a 3 mm thick HDPE sheet using a water-jet cutter. The thickness and stiffness of the inclusion were selected to minimize deformation and potential breakage of the ribs during testing. The inclusions differ in aperture size but share the same rib thickness. The ratio of the aperture width to particle size ( $A/D_{50}$ ) is 4 for H1 and 2.2 for H2.

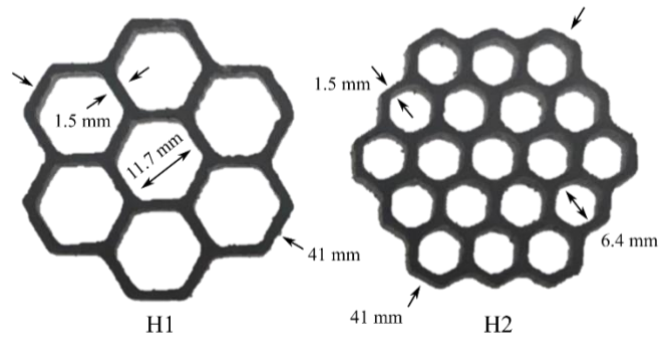


**Figure 2.** Honeycomb inclusions used for the stabilized tests.

## 2.4. Testing conditions

Stabilized triaxial samples measuring 50 mm in diameter and 100 mm in height were constructed inside a custom, transparent silicone membrane. Lubricated platens with drainage holes were used to reduce the ‘dead zones’ next to the platens (Head, 1986). These ‘dead zones’ had the potential to interfere with the stabilized zones to either side of the inclusions. Two layers of black silicone rubber, lubricated with vacuum grease, were used for each platen.

The specimens were tested under both monotonic and repeated loading. Each specimen was compacted in eight layers by tamping. A back pressure of 300 kPa was applied to dissolve potential air bubbles trapped between the particles and improve the transparency of the specimens. The B-value for all tests was in excess of 0.99. Five of the samples were sheared at a confining stress of 25 kPa. This confining stress was selected as a practical compromise between the comparatively low confining stress expected in a typical road base/subbase layer (Uzan, 1985; Selig, 1987) and test repeatability. A sixth specimen was sheared at a confining stress of 50 kPa to investigate the effect of confining stress.

Two repeat samples were monotonically sheared at a rate of 6% axial strain per hour to confirm the repeatability of the testing setup. The monotonically loaded tests were also used to determine the load levels to be adopted in the repeated load tests. These specimens had a post-consolidation void ratio of 0.70. The comparatively slow rate of shearing was required to facilitate pore pressure dissipation through the small drainage holes in the lubricated platens. Furthermore, a relatively slow shutter speed (0.4 s) was required when capturing the images, as the lasers were the only source of illumination. Thus, the sample had to be sheared slow enough such that no significant particle motion occurred while the shutter was open.

Four specimens were tested under repeated loading to measure the development of the stabilized zones next to the honeycomb inclusions. The first three specimens were consolidated to 25 kPa. Of these specimens, one was a control (non-stabilized), one stabilized with inclusion H1 and one stabilized with inclusion H2. The fourth specimen was stabilised with H1 but consolidated to 50 kPa (referred to as H1-50). The average void ratio of these four specimens was 0.72.

The repeated loading tests consisted of four stages. The first stage entailed five cycles of loading. In each cycle the specimen was loaded at a rate of 6%/hour up to the stress corresponding to 0.5% strain of the monotonic tests on the control specimens. The top platen and the loading ram were uncoupled

to avoid the development of tension during unloading. In the second stage, five cycles were applied up to the stress corresponding to 1% strain of the control tests. The third stage consisted of three additional cycles up to the stress corresponding to 2% axial strain. The number of cycles adopted in the testing program was selected to account for the slow loading rate as well as the large volume of image data generated per test. Finally, the specimens were monotonically sheared to the failure stress of the control specimens (140 kPa).

### **3. General image processing**

Alternating images were captured of the two laser-illuminated sections of the specimens during testing. For the monotonic shear test, the images were captured at increments of 0.02% axial strain. During the repeated loading tests the frequency was increased to 0.01%. A summary of the image processing pipeline is discussed below.

#### **3.1. Image pre-processing**

Images were stored in a 14-bit raw format during testing. After the raw images were demosaiced, a log transform was applied to compress the dynamic range of the image (Bovik, 2009). This transform enhanced the detail of the poorly illuminated particles and the pore space.

The single light source (the lasers) and heterogeneous refraction by the particles resulted in inconsistent exposure across the images. This was addressed by applying Contrast Limited Adaptive Histogram Equalization (CLAHE) to the images (Zuiderveld, 1994). The equalized images were then corrected for internal camera distortion as well as lens distortion (White et al., 2003).

LED markers on the alignment frames were used to centre the series of images. Finally, the images were corrected for the distortion caused by the convex triaxial cell wall, following the approach presented by Zhang et al. (2015). The result was a series of undistorted, aligned images with clearly visible particles and a known pixel-to-millimetre calibration factor.

#### **3.2. Digital image correlation**

Digital Image Correlation (DIC) is an optical technique used to measure full-field displacements of a series of images (Schreier et al., 2003). Typically, the images are divided into a series of adjacent or overlapping subsets (or patches). The position of these subsets is tracked throughout a test by searching for the location in the target image where the cross-correlation with the reference subset is maximized. Sophisticated algorithms, such as the GeoPIV-RG software (Stanier et al., 2016), used in this study, allow for the subsets to deform and rotate during a test.

In the tests conducted for the present study, the fused quartz particles were relatively large (~2.9 mm) in relation to the area of interest (~50 mm). This necessitated tracking relatively large subsets of ~10 mm in diameter to ensure that each subset contained at least three unique features, as recommend by Jones & Iadicola (2018). The overlapping subsets were spaced ~2.5 mm apart to provide a high-resolution measurement field. As each patch consists of multiple particles, individual particle displacement and rotation cannot be measured. Consequently, the images must be segmented into individual particles, as will be discussed in Section 4.

When testing triaxial specimens with lubricated ends, the global displacement measurements represent the compression of both the soil and the lubrication (Sarsby et al., 1982). Consequently, local strain measurements are required for an accurate representation of the axial strain (Clayton and Khatrush, 1986). The displacement fields from the DIC were used to construct virtual axial strain gauges (Marx and Zornberg, 2022). These gauges were positioned from the first to the last rows of patches that did not overlap with the drainage pipes in the lubricated platens.

## 4. Particle tracking

The result of a DIC analysis is a continuum displacement field. However, individual particle motions are required to study the complex, discrete interaction at the soil-inclusion interface. To measure individual particle displacement and rotation, the images were segmented using a neural network. These segmented particles were modelled as elliptical Fourier shape descriptors and subsequently matched between successive images.

### 4.1. Image segmentation

An extract of a typical image obtained during the triaxial testing is presented in **Figure 3a**. Several of the particles are sharply outlined by the refraction of the sheet laser. These outlines are classified as “ridges”, rather than “edges”, in image analysis. Specifically, “ridges” involve a sharp increase in pixel intensity from outside the particle to the top of the ridge, followed by a sharp decrease towards the centre of the particle. For an “edge”, the image intensity will only increase or decrease sharply, and then remain constant.

The use of analytical filters was attempted, but they failed in detecting particle outlines. As an example, the response of the ridge filter by Meijering et al. (2004) applied to a typical image of fused quartz particles is shown in **Figure 3**. This filter was originally developed to identify neurites and can also be used to delineate thin structures such as rivers and roads. However, due to inconsistent lighting, surface roughness, and image noise the particle outlines, and consequently the filter response, are discontinuous. Furthermore, the intensities of the particle outlines differed, resulting in an inconsistent filter response. The combination of these two factors made it infeasible to analytically derive continuous particle outlines. As an alternative, a convolutional neural network was used to segment the images.

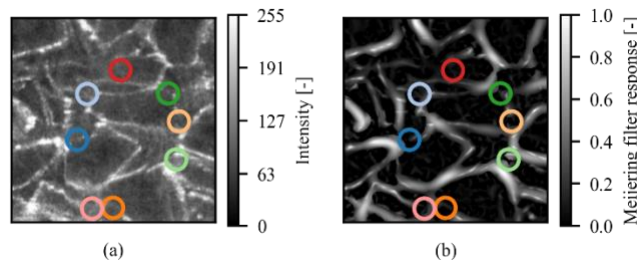


**Figure 3.** (a) A typical image of fused quartz along a laser illuminated plane. (b) Response of the Meijering filter. Discontinuities in the particle outlines are indicated with circles.

### 4.1.1. Convolution neural networks

A common form of neural networks is a series of logistic regression models stacked together (Murphy, 2012). For a single logistic model, the input layer  $\mathbf{x}$  is weighted with weights  $\mathbf{v}$ , summed and passed through an activation function  $g$ , such as the logistic function. The final non-linear function, known as an activation function, distinguishes these models from standard linear regression.

Multiple logistic models can be applied to the same input. When the output of these multiple logistic models is fed into a subsequent logistic model, as shown in **Figure 4**, it is known as a neural network (multi-layer perceptron). The intermediate activations are known as hidden nodes ( $\mathbf{z}$ ) and forms a hidden layer. A network with multiple hidden layers is defined as a deep neural network (Goodfellow et al., 2016).

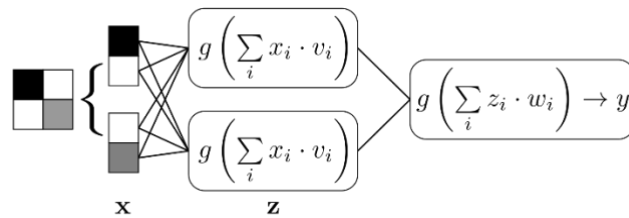


**Figure 4.** A multi-layer perceptron with two hidden nodes and a single output class.

For image applications a type of neural network known as a Convolutional Neural Network (CNN) is often used. In a fully connected network, such as the multi-layer perceptron in **Figure 4**, each input is connected to every node in the next layer. In contrast, a CNN creates sparse connections using convolution (Goodfellow et al., 2016).

**Figure 5** shows an input image  $\mathbf{x}$  convolved with a filter  $\mathbf{w}_k$ . During convolution with the 3x3 filter, a group of nine input pixels are multiplied with the nine weights of the filter and summed, providing one entry in the output array. The process is repeated across the image, resulting in a filtered image. The filtered image is passed through a non-linear activation function ( $g(\cdot)$ ), resulting in the feature map (or activation map) for that filter ( $\mathbf{A}_k$ ). Each convolutional layer typically consists of multiple filters. As only a subset of pixels contributes to each entry in a feature map, the connectivity of the network is sparse.

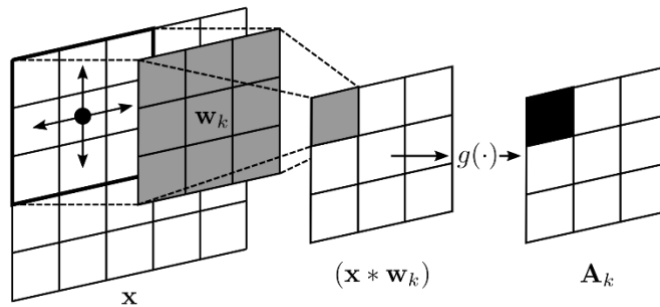


**Figure 5.** Convolution of an image with one filter

### 4.1.2. The Cellpose algorithm

Convolutional neural networks are the backbone of image segmentation with deep learning. One approach is to use the CNNs to classify each pixel in an image into a discrete number of classes. The pixels are then grouped according to class to segment the image. One such network architecture used for segmentation is U-Net (Ronneberger et al., 2015). A typical U-Net network is shown in **Figure 6**. The key characteristic of the network is an encoder ( $E_1$  to  $E_4$ ) followed by a decoder ( $D_4$  to  $D_1$ ).

The network shown in **Figure 6** consists of four scales for both the encoder and decoder. Each scale consists of several convolutional layers. During encoding the activation maps are down-sampled between scales using max pooling ( $E_1$  to  $E_4$ ). The max pooling operation involves grouping the feature maps into neighbourhoods of 2x2 pixels and reports the maximum. These max pooled feature maps are used as input for the next layer. Typically, the number of features (filters) doubles for each scale.

In the original U-Net version the last layer of the encoder ( $E_4$ ) is connected to the first layer of the decoder ( $D_4$ ) with convolution. For the decoder the input to each scale is the up-sampled output of the lower level combined with the output of the equivalent level of the encoder. The final feature maps are often passed to a fully connected layer to output the pixel classes.

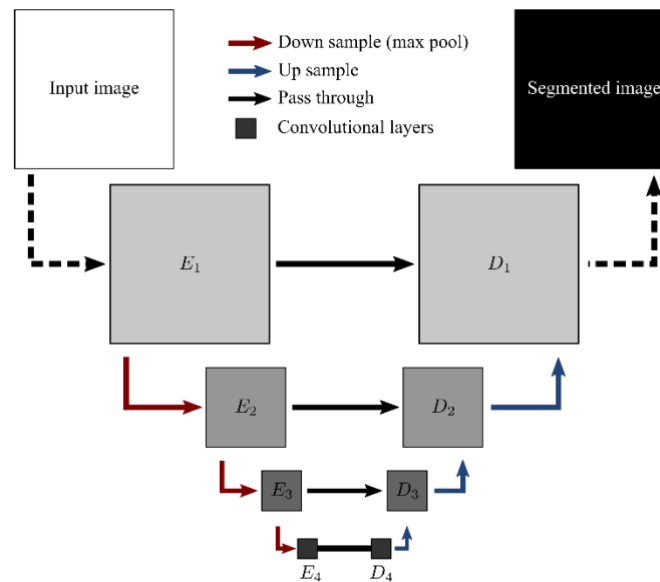


**Figure 6.** Key components of the U-Net architecture.

In the present study the Cellpose algorithm (Stringer et al., 2021) that is based on U-Net was used to segment the images of fused quartz. Cellpose was developed to segment biological tissues, which were found to share the same ridge-like characteristics as the fused quartz in the laser-illuminated sections. Alternative algorithms, such as Mask R-CNN (He et al., 2017) that first detects an object and then segments it, were also considered. However, these general-purpose models were found to perform comparatively worse than Cellpose due to the limited images available to train the networks to segment fused quartz specifically.



Conventional segmentation creates a topological map by considering the image intensities as elevations. The mounds in the map represent the regions to be segmented. However, as previously stated, the perimeters of the fused quartz particles in the triaxial tests formed ridges, rather than smooth mounds. To address this, Cellpose uses U-Net to predict a smooth topological map from an image and then proceeds to segment this intermediary map.

The topological map consists of so-called horizontal and vertical “flows.” These flows represent the horizontal and vertical diffusion gradient from a heat source placed at the centre of the particle. For each image the network predicts the flows at each pixel as well as the probability that a given pixel belongs to a particle. **Figure 7a** to **7d** show a typical input image and the predicted horizontal flow, vertical flow, and particle probability. All pixels with flows that converge at the same point (source) are grouped together as a particle during segmentation. Accordingly, the particles segmented from **Figure 7a** are shown in **Figure 7e**.

#### **4.1.3. Training and image augmentation**

The Cellpose models had been trained using a library of segmented images of biological cells. While these cells are similar to fused quartz particles, the accuracy of the network could be improved. Transfer learning was implemented, as manually generating segmented fused quartz images for training the model from the ground up was infeasible.

Transfer learning is based on the principle that models that perform similar functions on different datasets will share some general characteristics (Pan and Yang, 2010). Thus, a model trained to segment biological cells can be fine-tuned to segment fused quartz particles. Six images were manually segmented using the Cellpose graphical user interface, yielding a total of 3,100 unique particles. These images were sampled from both control and stabilized specimens, both after the consolidation and the shearing stages of the tests. In contrast to the DIC analysis, the performance of the network improved when the images were first denoised with total variation denoising (Getreuer, 2012).

A generalized model is one that performs well on data to which it has not previously been exposed. One technique to enhance the generalization of a model is data augmentation. Data augmentation assumes that the input images contain additional information that can be extracted (Shorten and Khoshgoftaar, 2019). By artificially inflating the dataset the generalizability of the model can be improved.

For the present study 12 augmented images were generated from each of the original six images, yielding a total of 72 training images. The original images were randomly rotated, flipped, cropped, resized, and the contrast and brightness were randomly adjusted. It is considered good practice to divide the input data into a training set, validation set and testing set (Goodfellow et al., 2016; Chollet, 2018). The first set is used to train the model, the second set to determine when to terminate training, and the final set to test the accuracy of the model. Seventy percent of the augmented images were used for training, 10% for validation and 20% for testing.

The ‘cyto2’ model of Cellpose (Stringer and Pachitariu, 2022) was trained for a further 750 epochs with the additional fused quartz images. An epoch involves iterating through the full training set, calculating the error (the training loss), and adjusting the weights. In addition, the error of the

prediction on the validation set is calculated. The validation loss was found to stabilize after 750 epochs. Any further training would result in overfitting of the model.

The training and validation loss are limited to the ability of the neural network to predict the horizontal and vertical flows for the image, and not the actual segmentation. Following Stringer et al. (2021), the accuracy  $A$  of the segmentation is defined as:

$$A = \frac{T_p}{T_p + F_N + F_p} \quad (1)$$

where  $T_p$  are the true positives;  $F_N$  are the false negatives; and  $F_p$  are the false positives. To determine whether a segmented particle is a true positive or a false positive the intersection over union (IoU) is calculated as follows:

$$IoU = \frac{A \cap B}{A \cup B} \quad (2)$$

Different threshold values of IoU can be used to define a true positive match. For the ‘cyto2’ model the segmentation accuracy for the testing dataset was 0.25 at the commonly used IoU threshold of 0.5. An IoU of 0.5 corresponds to two identical circles overlapping with 67%. For the model refined with the images of fused quartz the accuracy at an IoU of 0.5 increased to from 0.25 to 0.69.

#### 4.1.4. Explainable AI: Score-CAM

Deep neural networks consist of millions of trainable parameters, so they effectively become a “black box” for the user. Accordingly, the model user runs the risk that a model can make predictions based on features in an image that do not make physical sense. The emerging discipline of “Explainable AI” attempts to improve the transparency and trustworthiness of these models without compromising their high performance (Barredo Arrieta et al., 2020).

Each two-dimensional feature map in a CNN is activated by different characteristics of the image (e.g. ridges or empty space). Thus, different feature maps will be significant for a prediction depending on the class under consideration (e.g., particle or no particle). The sum of all the feature maps, weighted by their significance to a given class, results in a heatmap highlighting the regions of an image with the greatest contribution to the class under consideration.

To evaluate the explainability of the Cellpose network the Score-CAM (Wang et al., 2020) metric was calculated. For an image  $X$ , Score-CAM for a class  $c$  is defined as the sum of the  $k$  feature maps  $A^k$ , of layer  $l$ , weighted by their contribution  $\alpha_k^c$  to the class:

$$L^c = ReLU \left( \sum_k \alpha_k^c A_l^k \right) \quad (3)$$

where

$$\alpha_k^c = C(A_l^k) = f(X \circ H_l^k) - f(X_b) \quad (4)$$

and

$$H_l^k = s \left( Up(A_l^k) \right) \quad (5)$$

As presented by Equation 4, the contribution of a feature map ( $\alpha_k^c$ ) to a class is defined as the difference between the class output for a baseline image ( $f(X_b)$ ) and the output for an image where the features significant to class  $c$  are emphasized  $f(X \circ H_l^k)$ .  $H_l^k$  defined in Equation 5 is the feature map up-sampled ( $Up(\cdot)$ ) to the size of the image ( $X$ ) and normalized between 0 and 1 ( $s(\cdot)$ ). Finally, the weighted sum is passed through the Rectified Linear Unit operator (ReLU,  $f(x) = \max(0, x)$ ) because only positive contributions to a class are relevant.

For U-Net the feature maps of the convolutional layers of the encoder are typically the most insightful to analyse (Vinogradova et al., 2020). In **Figure 7f** to **7h** the Score-CAM metric is shown for a single pixel ( $\diamond$ ) of a particle, and corresponds to the three classes modelled by Cellpose for the output of the final convolutional layer of the encoder.

The vertical flows at the pixel are sensitive to the northern slope of the particle, the pore space, and the southern slope of the opposite particle. However, a few regions of the image unrelated to the specific pixel also contributed to the local prediction. Some of this inconsistency can be attributed to boundary effects. Nonetheless, the results do suggest that the model can be improved by increasing the training set or by improving the architecture of the network. The Score-CAM metric for the horizontal flows follows the same trend as that for the vertical flows. The probability that a pixel will fall inside a particle depends on the edges of the surrounding particles, as can be observed in **Figure 7h**. Therefore, the predictions by the Cellpose model are mostly grounded in the physical characteristics of the image. Consequently, the segmentation by the Cellpose algorithm is deemed rational for the images of fused quartz.

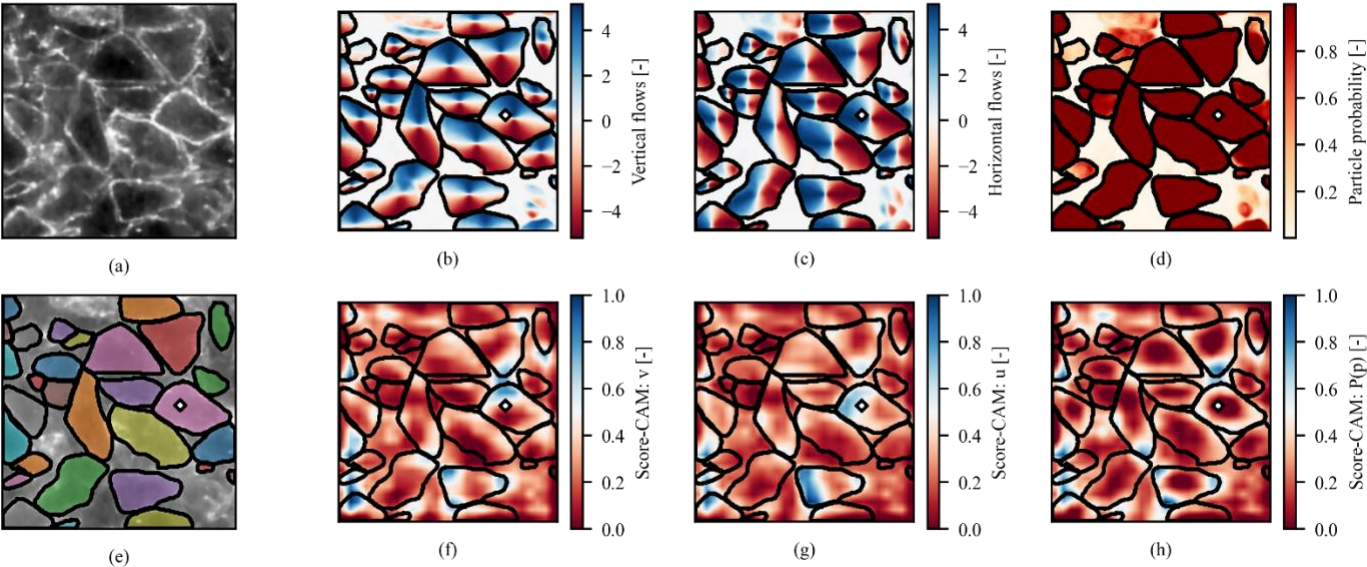


**Figure 7.** Cellpose demonstration: a) input image; b) vertical flows; c) horizontal flows; d) particle probabilities; e) segmented image; f) Score-CAM map for the indicated pixel for vertical flows; g) Score-CAM map for the indicated pixel for horizontal flows; and h) Score-CAM map for the indicated pixel for particle probabilities.

## 4.2. Fourier shape descriptors

Inconsistent lightning and out-of-plane particle rotation may result in minor differences in the particle outlines between consecutive images. To effectively track these fluctuating particles, global representations of particle shape known as Fourier descriptors (Burger and Burge, 2013), were adopted in this study.

A Fourier series represents a periodic function as an infinite sum of sine and cosine functions. To calculate the Fourier descriptors of a particle, discrete coordinates  $\mathbf{v}_k = (x_k, y_k)$  are sampled regularly along a particle's perimeter. These coordinates are then interpreted as points on the complex plane:  $\mathbf{g}_k = x_k + i \cdot y_k$ . Finally, the forward discrete Fourier transform of the complex plane is calculated (Burger and Burge, 2013):

$$G_m = \frac{1}{M} \cdot \sum_{k=0}^{M-1} [x_k + i \cdot y_k] \cdot \left[ \cos\left(\omega_m \frac{k}{M}\right) - i \cdot \sin\left(\omega_m \frac{k}{M}\right) \right] \quad (6)$$

where  $G_m$  is the Fourier shape descriptor for frequency  $m$ ;  $M$  is the signal length; and  $\omega_m = 2\pi m$ .

For the present study the variant of the Fourier shape descriptor calculation developed for polygons with arbitrarily spaced vertices was used (Burger and Burge, 2013).

In **Figure 8**, an original shape is displayed along with iterations reconstructed with an increasing number of Fourier descriptor pairs. The centroid of the shape,  $G_0$  is also indicated. For only one pair of descriptors ( $(G_{-1}, G_{+1})$ ), the reconstructed shape is the fundamental ellipse. As the number of descriptor pairs increases, the reconstructed shape represents the original shape in more detail. Thus, when calculating the Fourier descriptors of a fused quartz particle, the higher order coefficients will represent minor variations in the outline of a particle between two images. By filtering out these higher order coefficients, it is possible to match a particle despite fluctuations in the outline. In this study, nine Fourier descriptor pairs were established to be the optimal balance that allowed representing the essence of a particle without capturing too much detail.

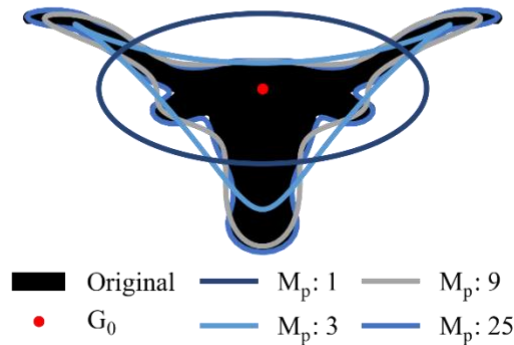


**Figure 8.** Shape reconstruction for increasing numbers of Fourier shape descriptor pairs.

Fourier analysis assumes that a signal is periodic, and closed particle boundaries are implicitly periodic. However, the Fourier descriptors may vary depending on where coordinates are sampled along the curve. Consequently, before matching the descriptors, they must be made invariant to the starting point. In addition, the descriptors were also made invariant to scale and rotation.

Complex (phase-preserving) matching was used to calculate the distance between the descriptors  $\mathbf{G}_1$  and  $\mathbf{G}_2$  of two given particles ( $FD_{dist}$ ):

$$FD_{dist}(\mathbf{G}_1, \mathbf{G}_2) = \left( \sum_{m=M_p, m \neq 0}^{M_p} |\mathbf{G}_1(m) - \mathbf{G}_2(m)|^2 \right)^{\frac{1}{2}} \quad (7)$$

The centroid ( $G_0$ ) was ignored during matching to make the coefficients invariant to translation.

### 4.3. Particle matching

The number of particles successfully segmented differed from image to image, mainly due to changes in lightning. To establish the reference particle locations for matching, all particles found in the first five images were concatenated. These reference particles were matched with subsequent images following a quasi-leapfrog updating scheme.

The distance calculated between two descriptors in Equation 5 is an arbitrary number. To determine what constitutes a good match, a threshold distance was established by calculating the distance between each pair of 500+ particles in a reference image. The 2.5<sup>th</sup> percentile of the resulting distribution of distances was 0.13 and the 50<sup>th</sup> percentile was 0.25. Two particles in subsequent images were considered a match if their centroids moved less than a specified tolerance (typically 0.1 mm per image) and the Fourier descriptors distance is less than 0.2. If the Fourier descriptor distance exceeded 0.15, the reference particle was updated to the median shape of the last five particles. Tracking of missing particles stopped once median displacement of the remaining particles reached 1.5 mm (approximately 50% of  $D_{50}$ ).

The Fourier descriptors were smoothed across images after matching to minimize local variations in shape. The shape and position of a missing particle in an image was linearly interpolated from the smoothed Fourier descriptors of the particle in the neighbouring images.

**Figure 9** presents the motions of two particles in the centre of a stabilized sample, located at different vertical positions and tracked over five cycles of loading. The effect of the load cycles is clearly visible in the vertical displacement of the particles. In addition, a comparatively smaller magnitude of vertical displacement can be observed for the particle closest to the inclusion. This hints at the stabilization effect caused by the presence of the inclusion.

The principal axes of a shape are defined as the axes coinciding with the minimum and maximum moments of inertia of the shape (Hearn, 1997). These axes were used as basis to calculate the rotation of the particles. The vertices for each particle were first reconstructed from the smoothed Fourier descriptors and then used to calculate the image moments following the method by Steger (1996). Subsequently, the principal axis was calculated from the image moments (Mukundan and

Ramakrishnan, 1998). At each position of the two particles, the principal axis as well as the change in rotation are also indicated in **Figure 9**.

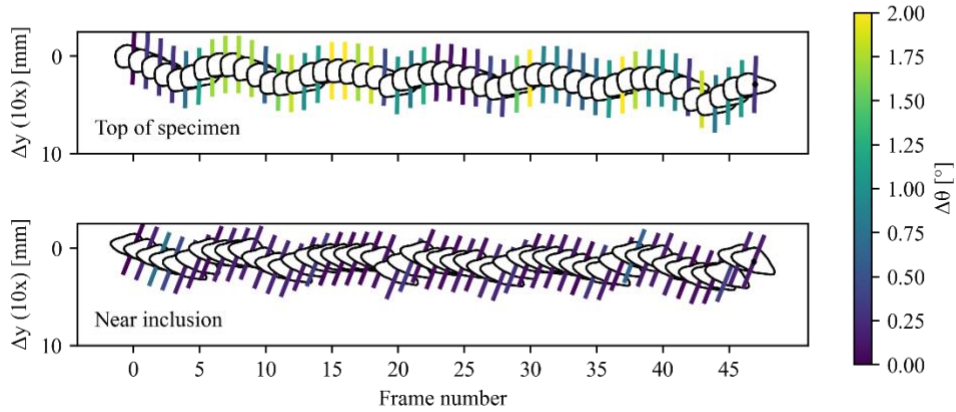


**Figure 9.** Tracking of individual particles in a stabilized test: (a) particle towards the top of the specimen; (b) particle in the vicinity of the inclusion

The principal axis is sensitive to variations in the outline of a particle. To quantify this sensitivity, the outlines of 650 particles were randomly varied and the change in the orientation of the principal axis was calculated. Each particle was reconstructed from the Fourier descriptors with 30 nodes, each of which were displaced in a random direction with a random magnitude sampled from a uniform distribution.

Ten permutations were created for each particle. For each permutation the displacement of the centroid, the change in principal axis orientation and the distance between the new and original Fourier descriptors were calculated. These values are summarised in Table 1 for three median magnitudes of node offset.

Table 1. Sensitivity of particle centroid and orientation to variations in outline.

Median node offset [mm]	Median centroid displacement [mm]	Median, absolute change in orientation [°]	Median distance in Fourier descriptors [-]
0.05	0.039	0.36	0.064
0.1	0.062	0.71	0.074
0.2	0.120	1.50	0.100

Considering the results of the sensitivity analysis, it was observed that when the distance in Fourier descriptors between a reference and target particle was 0.06, the resolution of the principal angle measurements was  $0.4^\circ$ . When  $FD_{dist}$  increases to 0.1, the resolution of the principal axis measurements worsens to  $1.5^\circ$ . For all three scenarios the resolution of the centroid displacement measurement was greater than the displacement imposed between two images (0.04% axial strain, i.e. 0.04 mm). Thus, the resolution of the axial strain measurements for the monotonic tests was on the order of 0.05% to 0.1% for  $FD_{dist}$  between 0.06 and 0.1.

## 5. Validation of experimental methodology

The two monotonically sheared specimens were used to confirm the repeatability of the specimen preparation procedure, the accuracy of the displacement measurements, and the repeatability of the rotation measurements.

**Figure 10** shows the stress-strain response of the two repeat triaxial specimens sheared monotonically. The stress was calculated considering the area corrections by Head (2014) and the membrane corrections by Duncan and Seed (1967). Volume reduction due to membrane penetrations was considered negligible (Hjortnaes-Pedersen and Molenkamp, 1982; Head, 2014). Shearing of transparent sand is prone to so-called “slip-stick” behaviour. Slip-stick involves brittle drops in deviatoric stress, followed by a gradual increase in load, and is postulated to be due to chains of load-bearing particles forming, collapsing, and reforming within the specimen (Ezzein and Bathurst, 2011). For the purpose of comparing the two repeat tests, these drops were filtered out of the stress-strain curves in **Figure 10**.

A good match was observed between the stress-strain responses of the two tests, confirming the repeatability of the test setup. In terms of volumetric behaviour, the samples matched up to  $\sim 7.5\%$  axial strain. Both samples dilated significantly during shear as a result of the highly angular nature of the particles, the low confining stress adopted for the tests, as well as a high specimen density.

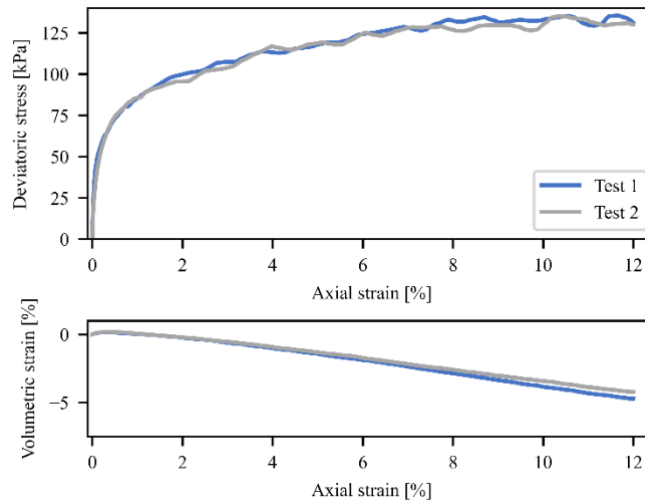


**Figure 10.** Stress-strain behaviour of the two monotonic tests.

The displacement fields generated using DIC were used to assess the accuracy of the particle displacement measurements. **Figure 11** displays the horizontal and vertical displacement contours after 7.5% axial strain for one of the monotonic tests. The segmented particles are overlaid on the DIC contours and shaded according to their displacement. For the particles shown in the figure, the median distance to the Fourier descriptors in the first image is 0.15. The relatively large  $FD_{dist}$  can be attributed to inconsistencies in lighting and out-of-plane particle rotation during the test.

Good correlation can be observed between the two methods of displacement measurement. The correlation coefficients for horizontal and vertical displacement are 0.87 and 0.99, respectively. At

2.5% axial strain the correlation between the horizontal displacement measurements is only 0.6 while the corresponding correlation for vertical displacement is 0.96. At these levels of axial strain, shear bands had not yet formed, and localized horizontal particle displacement may be haphazard. However, these localized displacements are smoothed by the large subsets in the DIC analysis, leading to poor correlation between the two measurement methods at low axial strain.

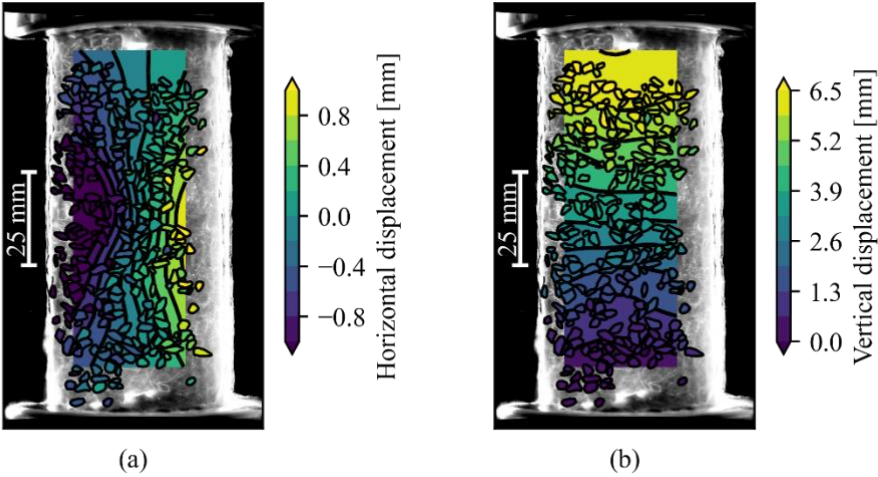


**Figure 11.** Validation of segmented particle displacement against displacements measured with DIC at 7.5% axial strain: a) horizontal displacement; and b) vertical displacement.

Particle displacements within a system of discrete particles is random by nature. Thus, to investigate mechanisms of soil-geogrid interaction based on particle rotation, the rotation measurements need to be repeatable across multiple specimens. **Figure 12** shows the median horizontal displacement and absolute particle rotation for two sections (East and West) of each of the monotonic tests. Only particles in the centre 25 mm of the sample were considered to minimize the impact of boundary effects.

In terms of horizontal displacement, all four sections follow the same general trend, and three sections show good agreement. For the rotation measurements, the four sections again follow the same trend, but with greater the variation between sections. This variation is attributed to the lower resolution of the rotation measurements, as well as the greater inherent variation in particle rotation throughout a test. Overall, the rotation measurements are deemed adequately repeatable to be used to investigate the mechanisms of soil-geogrid interaction.



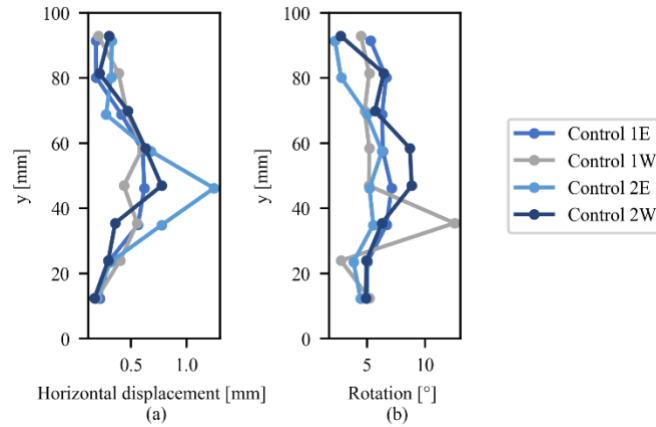


**Figure 12.** Comparison of particle motion in the monotonic tests at 7.5% axial strain: (a) horizontal displacements; (b) rotation.

## 6. Effect of the inclusions on particle displacement and rotation

### 6.1. Permanent axial and radial strain

**Figure 13** shows the accumulated axial, volumetric and radial strain after each load-unload cycle for the four specimens tested under repeated loading: a) control, b) stabilized with H1, c) stabilized with H2 and d) stabilized with H1 and tested at a confining stress at 50 kPa (H1-50). The axial strain was calculated from the virtual strain gauges while the volumetric strain was directly measured from the sample volume changes. The radial strain is shown for an equivalent right cylinder deformed with the axial strain  $\varepsilon_a$  and the volumetric strain  $\varepsilon_v$  at the end of each load-unload cycle.

During the first loading cycles, particles typically rearrange into a more compact state. In railway ballast settlement is classified into a non-linear compaction phase (“shakedown”) and a linear post-compaction phase (Jeffs and Marich, 1987; Dahlberg, 2001; Suiker et al., 2005). A significant decrease in the rate of axial strain accumulation after the first cycle can be observed for all the specimens. Thus, the first cycle of loading (Stage 0) was assumed to correspond to the “compaction” phase for the tests conducted in this study. The end of this load-unload cycle was considered the reference condition for subsequent calculations of rotation and displacement.

The stabilizing effect of the inclusions is apparent, as quantified by the reduced permanent axial strain for the H1, H2 and H1-50 specimens when compared to the control specimen across all cycles. Initially H1 and H2 behaved similarly. However, once the amplitude of the loading increased in Stage 2 and Stage 3, H2 showed less deformation than H1. As expected, specimen H1-50 deformed the least of the four tests due to the increased confining stress. H2 was loaded for an additional cycle during Stage 2 and the increase in permanent strain observed during this cycle was low enough to not warrant consideration in the following discussion.

All four specimens initially contracted during Stages 0 and 1, as shown by the results presented in **Figure 13b**. From the start of Stage 2 onwards, all three specimens tested at a confining stress of 25 kPa dilated. In contrast, specimen H1 continued to contract, which is consistent with the expected

behaviour of specimens tested higher confining stress. The most significant dilation occurred for the control specimen, as the particle motion was unrestricted.

The interplay of dilation, contraction and confinement by the inclusions confuses the interpretation of permanent volumetric strains for stabilized specimens H1 and H2, as presented in **Figure 13b**. A better understanding of the effect of the inclusions is gained from the radial strain shown in **Figure 13c**. For specimen H1-50, tested at a higher confining stress of 50 kPa, the radial strain is effectively zero. For the remainder of the specimens the trend in radial strain is consistent with that of the permanent axial strains: H2 strains less than H1, which in turn strains less than the control specimen. Thus, based on the permanent axial and radial strain measurements H2 can be considered the superior inclusion for these loading conditions.

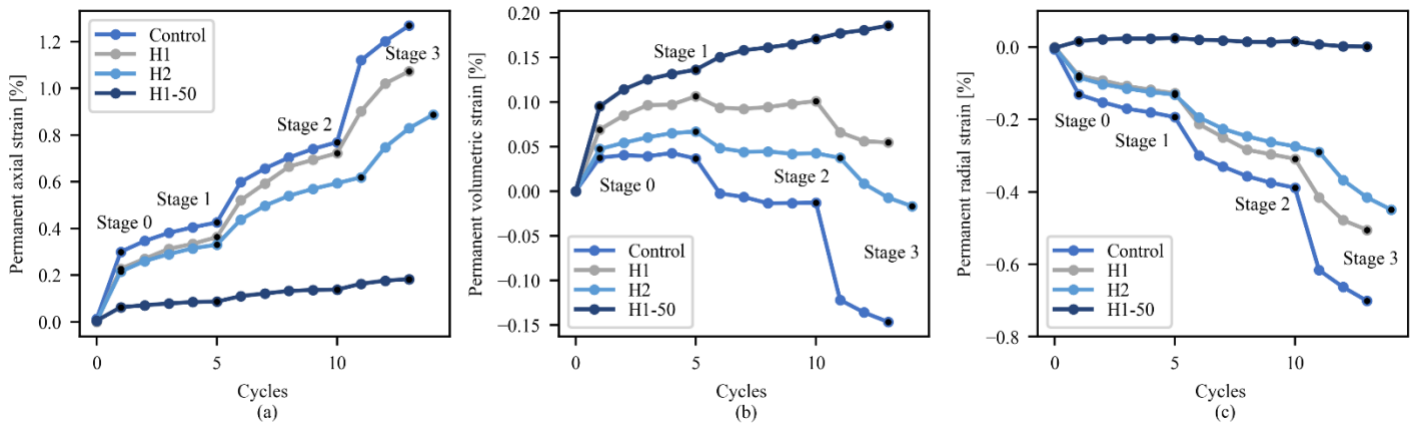


**Figure 13.** Accumulated strain in the specimens after each unloading cycle: a) axial strain, b) volumetric strain and c) radial strain. The end of each loading stage is also indicated.

## 6.2. Development of rotation and horizontal displacement

**Figure 14a** to **14f** show the horizontal displacement and rotation of individual particles as a function of depth for specimen H1 at the end of two stages of repeated loading (Stage 1 and 3), and the final stage of monotonic shear (Stage 4). The magnitude of displacement and rotation increase from Stage 1 to Stage 2, and from Stage 2 to Stage 3, is similar to the resolution of the measurements. Thus, only the particle motions for Stage 1, Stage 3, and Stage 4 (monotonic shear) will be compared. The axial strain at the end of the first three stages of loading is also indicated on **Figure 13**. At the end of Stage 4 (monotonic shear until failure of the control specimen at  $q = 140$  kPa) the axial strain was 8.7%, 2.8%, 2.8% and 0.5% for the control, H1, H2 and H1-50 respectively.

Particles near the membrane and platens, and those smaller than 1 mm in diameter were filtered from **Figure 14**. So were particles with Fourier descriptors further than 0.125, 0.15 and 0.2 from the reference image descriptors, respectively, for the three stages. This increase in the limit on  $FD_{dist}$  was necessitated by the greater rotation and corresponding decreased match quality with increased load. The median  $FD_{dist}$  values for the three stages shown in the figure are 0.06, 0.08, 0.1 respectively. This is equivalent to a resolution in displacement and rotation measurements of (0.04 mm, 0.4°), (0.08 mm, 0.9°) and (0.12 mm, 1.5°). The distances of the Fourier descriptors to the descriptors of the reference image are indicated on the colour bar.

The results provided in **Figure 14e** and 14f show an apparent trend of reduced rotations and displacements near the position of the inclusion. However, the large number of particles that does not follow this trend prevents a rigorous comparison of the behaviour of the different specimens as a function of depth only.

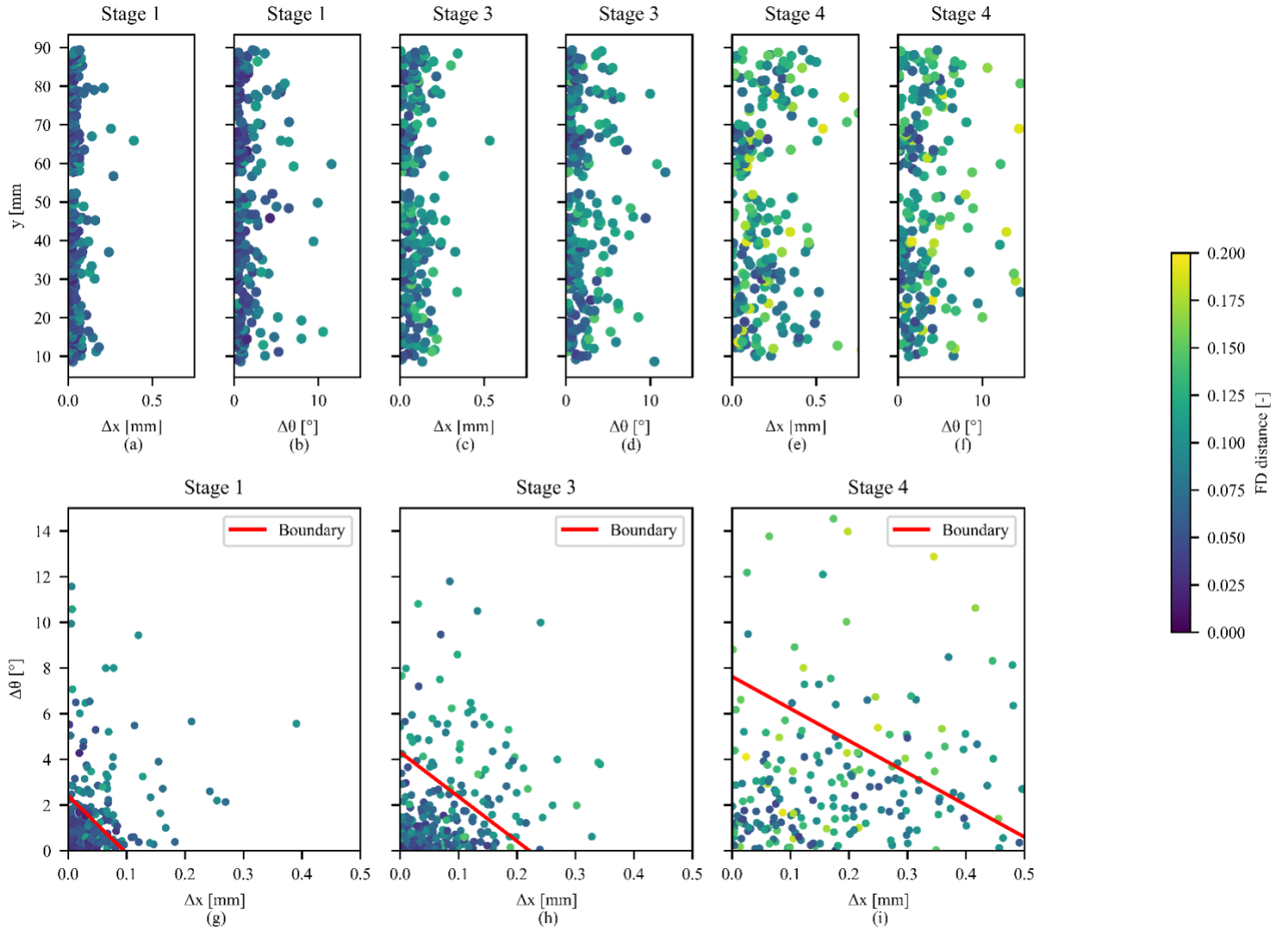


**Figure 14.** Horizontal displacement ( $\Delta x$ ) and rotation ( $\Delta \theta$ ) of the segmented particles for Specimen H1 over three different stages of loading. (a) to (f): rotation and displacement as a function of depth. (g) to (i): rotation as a function of displacement. The points are coloured based on the distance to the Fourier descriptors of the reference image.

Stabilized triaxial specimens are not unit cells due to the non-uniform stress state brought too by the inclusions. However, the results of soil-geosynthetic interaction tests conducted by Morsy et al. (2019) showed that the zone of influence by the geosynthetic extended to 150 mm for a granular material with a  $D_{50}$  of 7 mm. This would be consistent with a zone of influence of 62 mm for the granular particles tested in this study with a  $D_{50}$  of 2.9 mm. Thus, it can be argued that the full 100

mm of triaxial specimens were stabilized to some degree. As such, the global behaviour of the specimens be compared.

In **Figure 14g** to **14i** the rotation of the individual particles is shown as a function of horizontal displacement for the three stages of loading considered. The results in the figure indicate that the particles will generally either rotate or displace. Large displacement combined with large rotation may only be expected in particle arrangements that are unstable, which is not likely for these specimens that have not reached critical state. Thus, a boundary can be drawn separating probable states of displacement and rotation (motion) from improbable states of motion. In **Figure 14g** to **14i** such a boundary was drawn based on the Median of all Absolute Deviations from the median (MAD) (Rousseeuw and Hubert, 2018). The MAD is a robust estimate of the variability of the data and can be used to identify outliers as part of a z-score:

$$z = \frac{x_i - \text{median}(x)}{\text{MAD}(x)} < 2.5 \quad (8)$$

The displacement and rotation values for  $z = 2.5$  were used as the two intercepts for the boundary lines. The boundaries are sensitive to the selected z-value selected. Thus, the interpretation of the boundaries should be limited to establish trends rather than to obtain absolute values.

A clear increase in the limiting displacement and rotation values can be observed as the test progressed from loading Stage 1 (**Figure 14g**) to Stage 4 (**Figure 14i**). This corresponds to the increase in axial and radial strain in **Figure 13**. From Stage 3 to Stage 4, the displacement limit increases proportionally more than the rotation. That is, the slope of the boundary line becomes comparatively flatter. This indicates that particles are more likely to displace than rotate for the specimen stabilized with H1 at higher load levels.

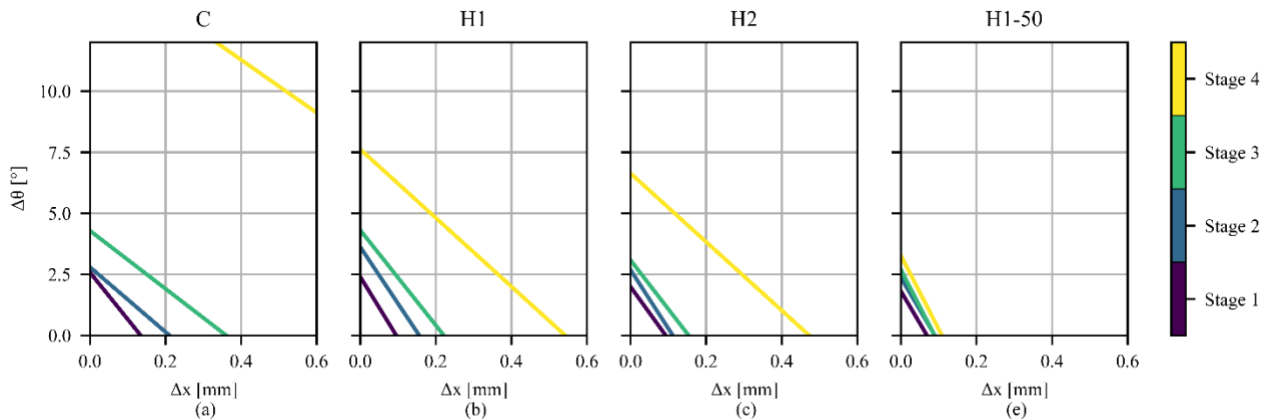


**Figure 15.** Development of horizontal displacement ( $\Delta x$ ) and rotation ( $\Delta \theta$ ) for the specimens across different stages of loading: a) control; b) stabilized with H1; c) stabilized with H2; and d) stabilized with H1 and tested at a confining stress of 50 kPa.

The development of the boundary between probable and improbable motions is shown in **Figure 15** for the four specimens investigated in this study. In **Figure 15** the zone of probable motions is smaller

for the stabilized specimens than for the control specimen, across all stages of loading. Thus, the inclusions restrict both the maximum particle rotation and displacement.

The zones of probable particle motions in **Figure 15** correlate with the trend in axial and radial strain presented in **Figure 13**. For example, H1-50 both strained less than H1, and the particle motions for H1-50 were restricted more than for H1. This improved performance of H1-50 in relation to H1 was due to the increase of 25 kPa in confining stress.

For two equivalent zones of probable motions, the stabilizing effect of a geogrid can be quantified in terms of an increase in confining stress. This increase in confining stress can be used to model the effect of geogrid stabilization in numerical or analytical models. For example, in Stages 3 and 4 the zone of probable motions for H2 is smaller than H1, but larger than H1-50. Thus, the effective additional confinement of particle motion due to the smaller apertures of H2, compared to H1, is less than 25 kPa for these two stages.

The zones of probable motion in **Figure 15** illustrate the difference in the mechanism of interaction between H1 and H2, for Stages 1 and 3. The rotation limit for H1 is similar to that of the control specimen. Thus, the reduced accumulated axial and radial strain for H1 in Stages 1 and 3, can primarily be attributed to the restriction in horizontal displacement of the particles. In contrast, both the rotation and displacement for particles stabilized with H2 are restricted compared to the control specimen. This may be due to the smaller apertures, which interlocks with a greater number of particles. However, for increased loading (Stages 3 and 4) the slope of the boundary line for all specimens becomes flatter, similar to **Figure 14g** to 14i. Thus, under increased load a particle will displace, rather than rotate.

For the set of results generated in this study at least, a ratio of aperture size to  $D_{50}$  of 2.2 (H2) proved to be more effective in stabilizing the specimens than a ratio of 4 (H1). This value differs from the generally reported optimal ratio of 3.5 between aperture size and  $D_{50}$  (e.g. Sarsby, 1985). However, the uniformly graded, angular sand tested in this study is more similar to ballast than the soils tested by Sarsby (1985). For ballast tested with rectangular geogrids, an optimum ratio on the order of 1 to 2 between aperture size and  $D_{50}$  has been reported (Brown et al., 2007; Indraratna et al., 2013), which aligns with the results of this study.

## 7. Conclusions

This study illustrated the successful combination of neural network image segmentation and triaxial tests on transparent soil to study soil-geogrid interaction. The Cellpose algorithm could be successfully trained to segment images of fused quartz with fair accuracy. By considering the Score-CAM metric from the field of Explainable AI it was shown that the network made rational predictions, even though it was originally developed to segment biological tissue. By defining particles in terms of their Fourier descriptors, particles could be tracked between images, despite minor variations in particle outlines. The individual particle displacement measurements were found to correlate with displacement fields calculated using digital image correlation. While the resolution of the particle rotation measurements was somewhat coarser, repeatable measurements were still achieved.

Three triaxial specimens were tested under repeated loading at a confining stress of 25 kPa, two of these specimens were stabilized with honeycomb inclusions. The honeycomb inclusions were used

as geogrid simulants that provided axisymmetric confinement. A fourth stabilized specimen was tested at a confining stress of 50 kPa. By tracking the individual particle motions, a boundary between probable and improbable displacement-rotation states (motions) could be identified. The size of the zone of probable motions decreased with increased confinement, whether due to stabilization by an inclusion or increased confining stress. A reduction in probable particle motions was found to correlate with reduced axial and radial strain of the specimens. For the uniformly graded fused quartz tested in this study, a ratio of aperture size to  $D_{50}$  of 2.2 was more effective in reducing strain and particle motion than a ratio of 4. Finally, the benefit of using the state-boundary to compare the performance of a stabilized specimen at a reference confining stress, against that of control specimens at different levels of confining stress was identified.

## Acknowledgement

The authors are grateful to Tensar International Corporation for the financial assistance provided for the study. Opinions expressed and conclusions presented are solely those of the authors.

## References

- Abdi, M.R., Mirzaeifar, H., 2017. Experimental and PIV evaluation of grain size and distribution on soil–geogrid interactions in pullout test. *Soils and Foundations* 57, 1045–1058.
- Alagiyawanna, A.M.N., Sugimoto, M., Sato, S., Toyota, H., 2001. Influence of longitudinal and transverse members on geogrid pullout behavior during deformation. *Geotextiles and Geomembranes* 19, 483–507.
- ASTM D4253-16, 2016. *Test Methods for Maximum Index Density and Unit Weight of Soils Using a Vibratory Table*. ASTM International.
- ASTM D4254-16, 2016. *Test Methods for Minimum Index Density and Unit Weight of Soils and Calculation of Relative Density*. ASTM International.
- Barredo Arrieta, A., Díaz-Rodríguez, N., Del Ser, J., Bennetot, A., Tabik, S., Barbado, A., Garcia, S., Gil-Lopez, S., Molina, D., Benjamins, R., Chatila, R., Herrera, F., 2020. Explainable Artificial Intelligence (XAI): Concepts, taxonomies, opportunities and challenges toward responsible AI. *Information Fusion* 58, 82–115.
- Black, J.A., Take, W.A., 2015. Quantification of Optical Clarity of Transparent Soil Using the Modulation Transfer Function. *Geotechnical Testing Journal* 38, 588-602.
- Bovik, A.C., 2009. *The essential guide to image processing*. Academic Press, London; Boston.
- Brown, S.F., Kwan, J., Thom, N.H., 2007. Identifying the key parameters that influence geogrid reinforcement of railway ballast. *Geotextiles and Geomembranes* 25, 326–335.
- Burger, W., Burge, M., 2013. *Principles of Digital Image Processing: Advanced Methods*. Springer-Verlag, London New York.

- Byun, Y.-H., Tutumluer, E., 2017. Bender Elements Successfully Quantified Stiffness Enhancement Provided by Geogrid–Aggregate Interlock. *Transportation Research Record* 2656, 31–39.
- Chollet, F., 2018. *Deep learning with Python*. Manning Publications Co, Shelter Island, New York.
- Clayton, C.R.I., Khatrush, S.A., 1986. A new device for measuring local axial strains on triaxial specimens. *Géotechnique* 36, 593–597.
- Coetzee, C.J., 2017. Review: Calibration of the discrete element method. *Powder Technology* 310, 104–142.
- Dahlberg, T., 2001. Some railroad settlement models—A critical review. *Proceedings of the Institution of Mechanical Engineers, Part F: Journal of Rail and Rapid Transit* 215, 289–300.
- Derksen, J., Fuentes, R., Ziegler, M., 2022. Geogrid-soil interaction: experimental analysis of factors influencing load transfer. *Geosynthetics International* 1–22.
- Duncan, J.M., Seed, H.B., 1967. Corrections for Strength Test Data. *J. Soil Mechanics and Foundations Division* 93, 121–137.
- Ezzein, F.M., Bathurst, R.J., 2011. A Transparent Sand for Geotechnical Laboratory Modeling. *Geotechnical Testing Journal* 36, 590–601.
- Getreuer, P., 2012. Rudin-Osher-Fatemi Total Variation Denoising using Split Bregman. *Image Processing On Line* 2, 74–95.
- Goodfellow, I., Bengio, Y., Courville, A., 2016. *Deep learning, Adaptive computation and machine learning*. The MIT Press, Cambridge, Massachusetts.
- Hall, S.A., Muir Wood, D., Ibraim, E., Viggiani, G., 2010. Localised deformation patterning in 2D granular materials revealed by digital image correlation. *Granular Matter* 12, 1–14.
- He, K., Gkioxari, G., Dollár, P., Girshick, R., 2017. Mask R-CNN. *Proceedings of the IEEE International Conference on Computer Vision*, pp. 2961–2969.
- Head, K.H., 2014. *Manual of soil laboratory testing*, 3rd ed.
- Hearn, E.J., 1997. Unsymmetrical Bending. In: *Mechanics of Materials 2*. Elsevier, pp. 1–27.
- Hjortnaes-Pedersen, A., Molenkamp, F., 1982. Accuracy and reproducibility of triaxial tests. *Deformation and Failure of Granular Materials*, Delft, pp. 391–401.
- Indraratna, B., Hussaini, S.K.K., Vinod, J.S., 2013. The lateral displacement response of geogrid-reinforced ballast under cyclic loading. *Geotextiles and Geomembranes* 39, 20–29.
- Jeffs, T., Marich, S., 1987. Ballast Characteristics in the Laboratory. *Proceedings of the Conference on Railway Engineering 1987*, Perth.
- Jones, E.M.C., Iadicola, M.A., 2018. *A Good Practice Guide for Digital Image Correlation*. International Digital Image Correlation Society.

- Kang, M., Kim, J.H., Qamhia, I.I.A., Tutumluer, E., Wayne, M.H., 2020. Geogrid Stabilization of Unbound Aggregates Evaluated Through Bender Element Shear Wave Measurement in Repeated Load Triaxial Testing. *Transportation Research Record* 2674, 113–125.
- Kharchafi, M., Dysli, M., 1993. Study of Soil-Geotextile Interaction by an X-Ray Method. *Geotextiles and Geomembranes* 12, 307–325.
- Marx, D.H, Zornberg, J.G., 2022a. Strain localization in a triaxial extension test on transparent sand. *Proceedings of the 7th International Young Geotechnical Engineers Conference*, Sydney, Australia, p. 6.
- McDowell, G.R., Harireche, O., Konietzky, H., Brown, S.F., Thom, N.H., 2006. Discrete element modelling of geogrid-reinforced aggregates. *Geotechnical Engineering* 159, 35–48.
- Meijering, E., Jacob, M., Sarria, J.-C.F., Steiner, P., Hirling, H., Unser, M., 2004. Design and validation of a tool for neurite tracing and analysis in fluorescence microscopy images. *Cytometry* 58A, 167–176.
- Morsy, A.M., Zornberg, J.G., Leshchinsky, D., Han, J., 2019. Soil–Reinforcement Interaction: Effect of Reinforcement Spacing and Normal Stress. *Journal of Geotechnical and Geoenvironmental Engineering* 145.
- Mukundan, R., Ramakrishnan, K.R., 1998. Geometric moments. *Moment Functions in Image Analysis: Theory and Applications*. World Scientific, Singapore, pp. 9–38.
- Murphy, K.P., 2012. *Machine learning: a probabilistic perspective*. MIT Press, Cambridge, MA.
- Ngo, N.T., Indraratna, B., Rujikiatkamjorn, C., 2014. DEM simulation of the behaviour of geogrid stabilised ballast fouled with coal. *Computers and Geotechnics* 55, 224–231.
- Peng, X., Zornberg, J.G., 2019. Evaluation of soil-geogrid interaction using transparent soil with laser illumination. *Geosynthetics International* 26, 206–221.
- Ronneberger, O., Fischer, P., Brox, T., 2015. U-Net: Convolutional Networks for Biomedical Image Segmentation. *Medical Image Computing and Computer-Assisted Intervention (MICCAI)*. Springer.
- Rousseeuw, P.J., Hubert, M., 2018. Anomaly detection by robust statistics. *WIREs Data Mining and Knowledge Discovery* 8.
- Sadek, S., Iskander, M.G., Liu, J., 2003. Accuracy of Digital Image Correlation for Measuring Deformations in Transparent Media. *Journal of Computing in Civil Engineering* 17, 88–96.
- Sarsby, R.W., 1985. The influence of aperture size/particle size on the efficiency of grid reinforcement. Proceedings of the Second Canadian Symposium on *Geotextiles and Geomembranes*. pp. 7–12.
- Sarsby, R.W., Kalteziotis, N., Haddad, E.H., 1982. Compression of “free-ends” during triaxial testing. *Journal of the Geotechnical Engineering Division* 108, 83–107.



- Schreier, H., Orteu, J.-J., Sutton, M.A., 2009. *Image Correlation for Shape, Motion and Deformation Measurements*. Springer US, Boston, MA.
- Selig, E.T., 1987. Tensile zone effects on performance of layered systems. *Géotechnique* 37, 247–254.
- Shorten, C., Khoshgoftaar, T.M., 2019. A survey on Image Data Augmentation for Deep Learning. *Journal of Big Data* 6, 60.
- Stanier, S.A., Blaber, J., Take, W.A., White, D.J., 2016. Improved image-based deformation measurement for geotechnical applications. *Canadian Geotechnical Journal* 53, 727–739.
- Stanier, S.A., Black, J.A., Hird, C.C., 2012. Enhancing accuracy and precision of transparent synthetic soil modelling. *International Journal of Physical Modelling in Geotechnics* 12, 162–175.
- Steger, C., 1996. *On the Calculation of Arbitrary Moments of Polygons* (No. FGBV–96–05). Forschungsgruppe Bildverstehen (FG BV), Informatik IX Technische Universität at München.
- Stringer, C., Pachitariu, M., 2022. Cellpose 2.0: how to train your own model. *BioRxiv*. Cold Spring Harbor Laboratory.
- Stringer, C., Wang, T., Michaelos, M., Pachitariu, M., 2021. Cellpose: a generalist algorithm for cellular segmentation. *Nature Methods* 18, 100–106.
- Suiker, A.S.J., Selig, E.T., Frenkel, R., 2005. Static and Cyclic Triaxial Testing of Ballast and Subballast. *Journal of Geotechnical and Geoenvironmental Engineering* 131, 771–782.
- Uzan, J., 1985. Characterization of granular material. *Transportation Research Record* 1022, 52–59.
- Vinogradova, K., Dibrov, A., Myers, G., 2020. Towards Interpretable Semantic Segmentation via Gradient-Weighted Class Activation Mapping (Student Abstract). *Proceedings of the AAAI Conference on Artificial Intelligence* 34, 13943–13944.
- Wang, H., Wang, Z., Du, M., Yang, F., Zhang, Z., Ding, S., Mardziel, P., Hu, X., 2020. Score-CAM: Score-Weighted Visual Explanations for Convolutional Neural Networks. *2020 IEEE/CVF Conference on Computer Vision and Pattern Recognition Workshops (CVPRW)*, Seattle, WA, USA, pp. 111–119.
- White, D.J., Take, W.A., Bolton, M.D., 2003. Soil deformation measurement using particle image velocimetry (PIV) and photogrammetry. *Géotechnique* 53, 619–631.
- Zhang, X., Li, L., Chen, G., Lytton, R., 2015. A photogrammetry-based method to measure total and local volume changes of unsaturated soils during triaxial testing. *Acta Geotechnica*. 10, 55–82.
- Zhou, J., Chen, J.-F., Xue, J.-F., Wang, J.-Q., 2012. Micro-mechanism of the interaction between sand and geogrid transverse ribs. *Geosynthetics International* 19, 426–437.
- Zuiderveld, K., 1994. Contrast limited adaptive histogram equalization. *Graphics Gems IV*. pp. 474–485.